Radar mapping of Mercury's polar anomalies

J. K. Harmon*, M. A Slade†, R. A. Vélez*, A. Crespo*, M. J. Dryer* & J. M. Johnson*

* National Astronomy and Ionosphere Center, Arecibo, Puerto Rico 00613, USA
† Jet Propulsion Laboratory, California Institute of Technology, Pasadena, California 91109, USA

GROUND-based radar observations of Mercury have revealed unusually strong, highly depolarized echoes from the north[1,2] and south[2] poles. These anomalous echoes have been cited as evidence of polar ice deposits[1–5]. Thermal studies[3–5] suggest that the permanently shaded floors of large polar craters are cold enough to preserve water ice in a stable state over aeons, in spite of Mercury's proximity to the Sun. Here we present high-resolution radar maps of Mercury's polar regions, derived from delay-Doppler measurements. We have resolved the north and south polar anomalies into numerous crater-sized features, and we have been able to identify the source craters for many of these features after making small corrections to the pole positions on the Mariner-10 images. The coincidence with crater locations, together with other properties of the radar features, are consistent with the polar-ice hypothesis.

In a preliminary report of Arecibo radar results[2] we showed that the south polar anomaly was mostly confined to the large crater Chao Meng-Fu. At the north pole the evidence was not so tidy. The north polar anomaly was clearly too large to fit within a single crater and had an offset from the pole that placed most of it within the 'unphotographed' hemisphere (the night side at the time of the Mariner-10 encounters).

Since reporting these initial results we have vastly improved the quality of the polar radar images by making new observations and by reanalysing and summing the original data. The data were obtained with the Arecibo Observatory's S-band (2.4-GHz) radar in three observing campaigns during 1991–92. The observations used a phase-coded transmission with a 100-μs delay resolution, giving a mapping resolution at the poles of 15 km in the line-of-sight (delay) coordinate. We achieved the same 15-km resolution in the transverse (Doppler) coordinate by quadrupling the length of the Fourier transform used in the spectral analysis from our original[2] 8,192 elements to 32,768 elements. (For details on the observations and analysis see ref. 2 and papers cited therein.) A mapping was done from delay-Doppler to planetary coordinates to give a polar projection image of radar cross-section per unit surface area (that is, specific cross-section σ_0) for each 25-min observing run. The polar images from various runs were then summed to reduce the statistical fluctuations from background noise. The north polar image (Fig. 1*a*) was formed by summing 27 observing runs; 16 of these runs were from the original eight observing dates[2] between 31 July and 29 August 1991, and the remaining 11 runs were from a new set of follow-up observations made on six dates between 19 July and 8 August 1992. The south polar image (Fig. 1*b*) is the sum of 16 runs obtained on eight dates between 14 March and 29 March 1992. Both images in Fig. 1 show the echo in the depolarized sense of circular polarization.

Figure 1*a* shows that most of the north polar anomaly is concentrated in crater-size (15–60 km) bright spots. We have plotted these features on the locating map in Fig. 2*a* and have given letter labels to those features that lie in the photographed hemisphere and to three prominent features in the unphotographed hemisphere. The brightest of the northern spots (D, E, H, J, K) roughly delineate the elongated and offset form of the unresolved anomaly as seen in the plane-of-sky images of Harmon and Slade[2]. The image also shows a score of fainter spots as well as a diffuse patchiness that extends along the 330° W meridian. (Further observations may determine whether

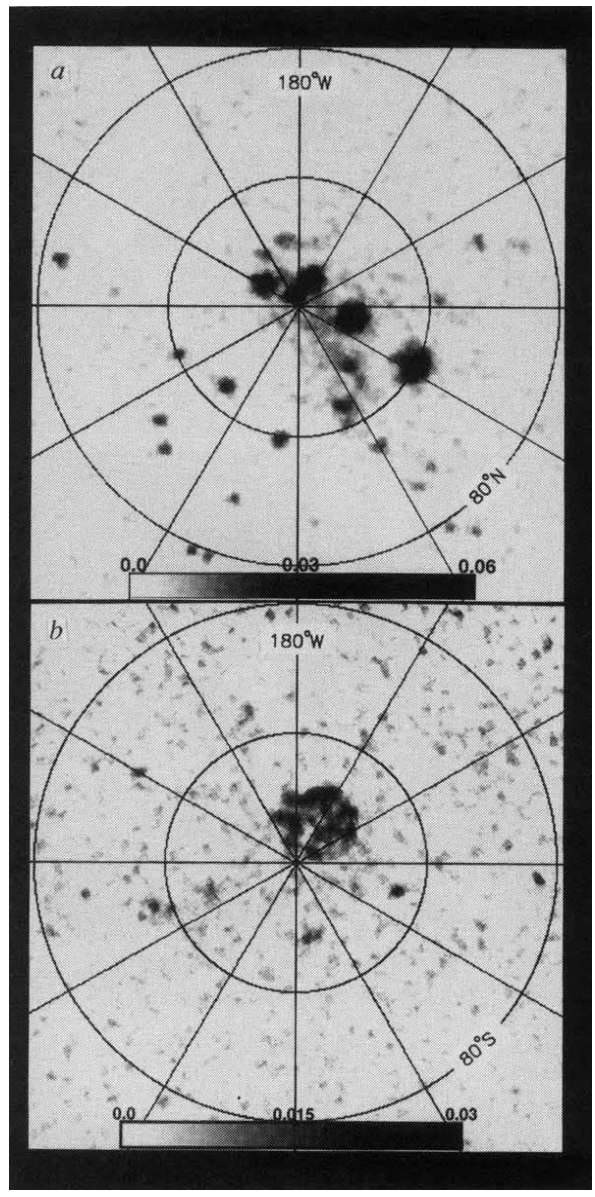

FIG. 1 Arecibo 2.4-GHz radar images of Mercury: *a*, north pole; *b*, south pole. The images show specific cross-section σ_0 (as given by the grey scale at the bottom of each panel) in the depolarized sense of circular polarization. The resolution is 15 km (0.35°). Note that the maximum value of σ_0 is 0.060 in *a* and 0.030 in *b*. The r.m.s. noise level is 3.5% of the maximum in *a* and 10.4% of the maximum in *b*.

the latter is truly diffuse or simply a dense collection of unresolved spots.) A comparison of the feature positions in Fig. 2*a* with the Mariner-10 image in Fig. 2*b* shows that by sliding the NASA/USGS coordinate grid in Fig. 2*b* down by 1.6° of latitude (along the 0° W meridian) one can get all of the features in the left half of the image to fall on or near known craters. The possibility that this is mere coincidence can be discounted, especially as many of these craters (for example, L–W) are located in an otherwise sparsely cratered region. The required 1.6° shift must represent an error in the NASA/USGS grid[6–8] rather than in our radar grid because the delay-Doppler mapping gives positions relative to the true pole with an accuracy of ~0.05°. Our results relocate the north pole to the southeastern rim of crater E (see Fig. 2*b*).

Figure 1*b* shows that the south polar echo is dominated by a 125-km-diameter circular feature (X) lying tangent to the pole. Sliding the NASA/USGS grid by 1.2° to the right (along the 90° W meridian) places feature X entirely inside Chao Meng-Fu

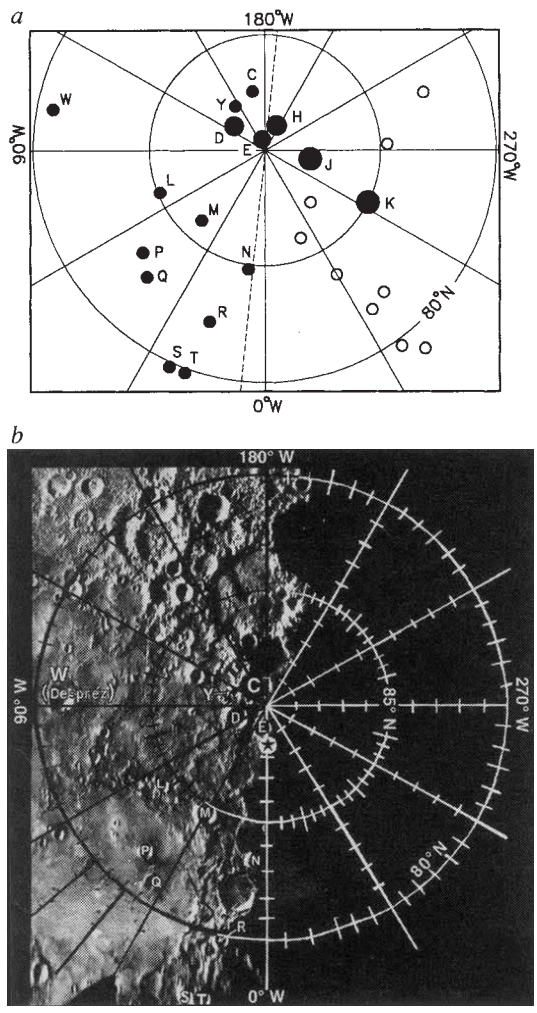

FIG. 2 Locating maps for north polar radar features. *a*, Locations of the letter-labelled features (filled circles) as well as some unlabelled features in the unphotographed hemisphere (open circles). The dashed line shows the location of the Mariner-10 terminator, the unphotographed hemisphere being to the right. *b*, Mariner-10 image of the north pole. Craters identified with radar features are given the same letter labels as in *a*. The coordinate grid in *b* is adapted from the NASA/USGS shaded relief maps[6–8]. There may be small discrepancies between the grid in *b* and the NASA/USGS grid due to distortions in the Mariner-10 image mosaics; there may therefore be differences between the crater positions in *b* and the crater coordinates listed in Table 1. Such distortions may also account for the tendency of the offsets between the radar features and source craters (for example, R, S, T) to increase near the bottom of the image. Our estimate of the true north pole position is shown in *b* (star).

crater and places features G, U and V inside other known craters (compare Fig. 3*a* and *b*). This grid shift also moves the south pole to a position which is in better agreement with the location of the Mariner-10 terminator (see Fig. 3*b*).

We stress that the proposed grid shifts represent readjustments of the NASA/USGS grid on the Mariner 10 images and not a new determination of the pole direction in the sky. The radar images (and grid) were calculated assuming zero polar obliquity and tests (in which the assumed pole direction was varied) showed that the zero-obliquity case gave minimum smearing of features in the summed images. Also, our proposed grid adjustments seem reasonable given that the NASA/USGS maps quote discrepancies of up to 40 km (1.0°) with respect to the Mercury control net and given that the control net itself has a standard error of 25 km (0.6°) at the north pole[7,13].

All of the geologically classified source craters in the north (C, D, E, M, N, R, T, W), as well as Chao Meng-Fu, have been mapped[8,9] as c_4-class (a USGS designation for craters that appear relatively pristine). Apparently the more degraded (and presumably older) craters do not contain near-surface deposits of radar-bright material.

In Table 1 we list the positions of the lettered radar features and their corresponding craters along with several parameters; (1) $\hat{\sigma}_p$, the peak feature reflectivity, (2) $\hat{\sigma}_a$, the feature's total depolarized cross-section divided by the mean area of crater floor that is both permanently shaded and radar-visible, (3) μ_c, the circular polarization ratio. Both reflectivity parameters ($\hat{\sigma}_p$, $\hat{\sigma}_a$) have been reduced to equivalent full-disk albedos to correct for incidence angle and enable comparison with other measurements. If the anomalies are enhanced back-scatter from ice then we might expect $\hat{\sigma}_p$ and $\hat{\sigma}_a$ to have values of a few tenths or so and $\mu_c > 1$ based on results from other icy bodies. (As the calculation of $\hat{\sigma}_a$ includes the stringent constraints imposed by the polar geometry, it serves as a particularly powerful test of the icy-crater hypothesis.)

The $\hat{\sigma}_p$ values indicate albedos of ~0.5 for the brighter features, which is two orders of magnitude higher than the disk-averaged depolarized albedo of the planet. For comparison, the depolarized albedos of the icy galilean satellites are in the range 0.4–1.6 (ref. 10) and the equivalent albedo of Mars' south polar icecap is 0.7 (refs 11, 12). The comparably high, but reasonable,

TABLE 1 Parameters of polar radar features/craters

Feature	Feature coordinates (°W, °N/°S)	Crater coordinates (°W, °N/°S)	$\hat{\sigma}_p$	$\hat{\sigma}_a$	μ_c
C	168W, 87.4N	133W, 89.1N	0.21	0.09	0.96±0.14
D	128W, 88.3N	66W, 88.5N	0.60	0.61	1.25±0.09
E	165W, 89.5N	12W, 88.8N	0.44	0.94	1.30±0.10
G	75W, 86.0S	78W, 84.9S	0.30	0.14	1.34±0.57
H	205W, 88.8N		0.53		1.15±0.09
J	281W, 88.0N		0.48		1.38±0.09
K	297W, 85.0N		0.27		1.30±0.10
L	68W, 85.1N	52W, 84.2N	0.21	0.65	1.19±0.25
M	42W, 85.9N	30W, 84.7N	0.28	0.28	1.24±0.17
N	8W, 84.8N	4W, 83.2N	0.20	0.39	1.20±0.18
P	50W, 83.1N	41W, 81.8N	0.15	0.34	1.50±0.47
Q	43W, 82.5N	35W, 81.0N	0.12	0.29	1.74±0.64
R	18W, 82.2N	12W, 80.0N	0.12	0.21	0.94±0.22
S	24W, 79.8N	16W, 77.8N	0.09	0.27	1.62±0.76
T	20W, 79.8N	13W, 78.1N	0.07	0.16	1.52±0.73
U	13W, 87.1S	30W, 86.4S	0.21	0.07	1.25±0.45
V	86W, 80.7S	86W, 79.8S	0.17	0.27	1.43±1.16
W	101W, 80.7N	92W, 81.0N	0.28	0.45	1.27±0.35
X	150W, 88.3S	133W, 87.5S	0.67	0.35	1.12±0.09
Y	146W, 87.8N	112W, 88.4N	0.23	1.15	1.66±0.45

The letter designations for C, D, E, G follow the crater naming convention in Paige *et al.*[3]; no radar features have been seen for their craters A, B, F. The only craters with proper IAU names are W (Despréz) and X (Chao Meng-Fu). The feature coordinates give the centre of the radar feature on the radar-based grid, while the crater coordinates give the position of the centre of the identified source crater on the NASA/USGS shaded relief maps[6–9]. Most of the difference between the two positions is apparently due to small pole-position errors or scale distortions in the shaded relief maps. The other parameters are; (1) $\hat{\sigma}_p$, the peak feature reflectivity, (2) $\hat{\sigma}_a$, the feature's total depolarized cross-section divided by the mean area of crater floor that is both permanently shaded and radar-visible, and (3) μ_c, the feature's total depolarized cross-section divided by its total polarized cross-section. Both $\hat{\sigma}_p$ *and* $\hat{\sigma}_a$ are given as equivalent full-disk albedos; they were calculated from the specific cross section σ_0 using $\hat{\sigma} = 2\sigma_0/(n+1)\cos^n\theta$ and assuming an $n = 3/2$ cosine scattering law (θ is incidence angle). The $\hat{\sigma}_a$ calculation assumed that the craters have flat floors, perpendicular walls, and a depth/diameter relation $d = 0.410D^{0.490}$ ($D < 30$ km) and $d = 0.353D^{0.496}$ ($D > 30$ km). Also, the shadow calculation assumed the Sun to be a point source, so some penumbral illumination is included. $\hat{\sigma}_p$ is 5–29 standard deviations above the noise background for the northern features and 5–10 standard deviations above the noise for the southern features. The error quoted for μ_c is one standard deviation.

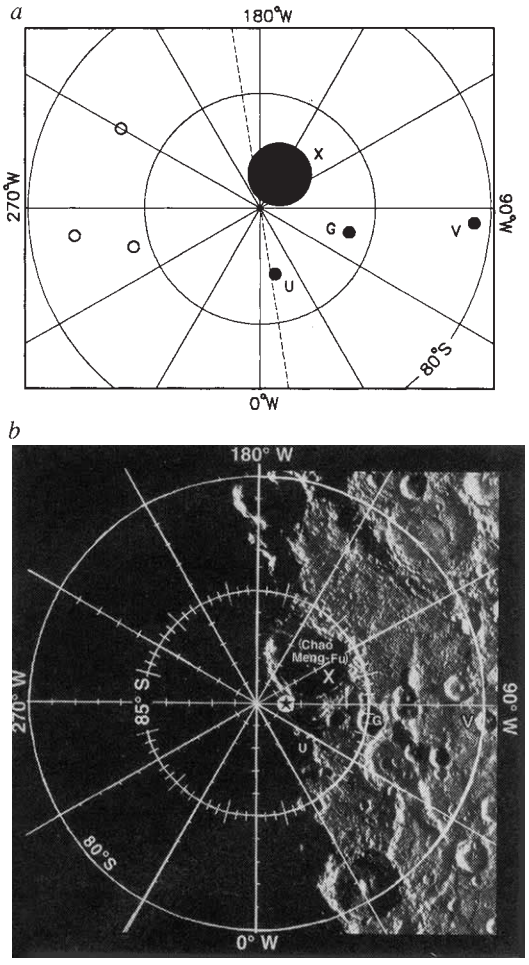

FIG. 3 Locating maps for south polar radar features. *a*, Locations of the letter-labelled features (filled circles) as well as some unlabelled features in the unphotographed hemisphere (open circles). The dashed line shows the location of the Mariner-10 terminator, the unphotographed hemisphere being to the left. *b*, Mariner-10 image of the south pole. There may be small discrepancies between the grid in *b* and the NASA/USGS grid due to distortions in the Mariner-10 image mosaics; there may therefore be differences between the crater positions in *b* and the crater coordinates listed in Table 1. Our estimate of the true south pole position is shown in *b* (star).

values of $\hat{\sigma}_a$ suggest that all of the identified source craters have enough shaded, radar-visible area to account for the high cross-sections. This seems to be the case even for features with latitudes as low as 80–81° (features S, T, V, W). However, permanent shadowing alone may not guarantee temperatures low enough to sustain ice[3,4], and additional theoretical work should be done to evaluate the plausibility of ice existing at these lower latitudes. Finally, Table 1 shows that the radar polarization of the features tends to be 'inverted' ($\mu_c > 1$); for the strongest of the features the measured inversion is statistically significant. Such polarization inversion is consistent with the X-band radar results for Mercury's north polar anomaly[1] and is reminiscent of the anomalous radar polarization of the icy galilean satellites[10] and Mars' southern icecap[11].

Our new images prove the connection between the radar anomalies and polar craters, and provide strong support for the notion that the radar-bright material is concentrated in permanently shaded crater floors. The most plausible model still seems to be one in which shaded crater floors act as cold traps for water ice, thick deposits of which provide a low-loss medium for enhanced volume backscatter of radio waves. Conclusive proof of the existence of polar ice will require spacecraft missions equipped with ultraviolet or neutron spectrometers and, possibly, sampling penetrators. The next mission to Mercury could, at the very least, provide the photoimaging necessary to (1) corroborate the cartographic grid refinements proposed here, and (2) identify source craters for those radar-bright spots which are presently located in unphotographed terrain. □

Received 22 February; accepted 5 April 1994.

1. Slade, M. A., Butler, B. J. & Muhleman, D. O. *Science* **258,** 635–640 (1992).
2. Harmon, J. K. & Slade, M. A. *Science* **258,** 640–643 (1992).
3. Paige, D. A., Wood, S. E. & Vasavada, A. R. *Science* **258,** 643–646 (1992).
4. Ingersoll, A. P., Svitek, T. & Murray, B. C. *Icarus* **100,** 40–47 (1992).
5. Butler, B. J., Muhleman, D. O. & Slade, M. A. *J. geophys. Res.* **98,** 15003–15023 (1993).
6. Davies, M. E., Dwornik, S. E., Gault, D. E. & Strom, R. G. *Atlas of Mercury* (NASA, Washington DC, 1978).
7. *Shaded Relief Map of Mercury* (USGS Map I-1149, US Geological Surv., Reston, Virginia, 1979).
8. Grolier, M. J. & Boyce, J. M. *Geologic Map of the Borealis Region of Mercury* (USGS Map I-1660, US Geological Surv., Reston, Virginia, 1984).
9. Strom, R. G., Malin, M. C. & Leake, M. A. *Geologic Map of the Bach Region of Mercury* (USGS Map I-2015, US Geological Surv., Reston, Virginia, 1990).
10. Ostro, S. J. *et al. J. geophys. Res.* **97,** 18227–18244 (1992).
11. Muhleman, D. O., Butler, B. J., Grossman, A. W. & Slade, M. A. *Science* **253,** 1508–1513 (1991).
12. Harmon, J. K., Slade, M. A. & Hudson, R. S. *Icarus* **98,** 240–253 (1992).
13. Davies, M. E. & Batson, R. M. *J. geophys. Res.* **80,** 2417–2430 (1975).

ACKNOWLEDGEMENTS. We thank R. Thomas, A. Venkataraman and P. Perillat for their assistance with computing. Ephemerides for the radar observations were supplied by the Center for Astrophysics. M.J.D. and J.M.J. were supported by the Arecibo summer student programme under a grant from the REU program of the US NSF. Part of this work was carried out under contract with NASA. The National Astronomy and Ionosphere Center (Arecibo Observatory) is operated by Cornell University under a cooperative agreement with the US NSF and with support from NASA.

Experimental observation of self-replicating spots in a reaction–diffusion system

Kyoung-Jin Lee*, William D. McCormick*, John E. Pearson† & Harry L. Swinney*

* Center for Nonlinear Dynamics and the Department of Physics, The University of Texas, Austin, Texas 78712, USA
† Center for Nonlinear Studies, Los Alamos National Laboratory, Los Alamos, New Mexico 87545, USA

IN his classic 1952 paper, Turing[1] suggested a possible connection between patterns in biological systems and patterns that could form spontaneously in chemical reaction–diffusion systems. Turing's analysis stimulated considerable theoretical research on mathematical models of pattern formation, but Turing-type patterns were not observed in controlled laboratory experiments until 1990[2,3]. Subsequently there has been a renewed interest in chemical pattern formation and in the relationship of chemical patterns to the remarkably similar patterns observed in diverse physical and biological systems[4]. Numerical simulations of a simple model chemical system have recently revealed spot patterns that undergo a continuous process of 'birth' through replication and 'death' through overcrowding[5]. Here we report the observation of a similar phenomenon in laboratory experiments on the ferrocyanide–iodate–sulphite reaction. Repeated growth and replication can be observed for a wide range of experimental parameters, and can be reproduced by a simple two-species model, suggesting that replicating spots may occur in many reaction–diffusion systems.

The laboratory chemical patterns form in a thin transparent gel (0.4 mm thick, 22 mm diameter) whose bottom surface is in contact with a well-stirred reservoir (3.0 ml volume) that is continuously refreshed with the reagents of the reaction[6]. Transitions are studied by changing the input ferrocyanide concentration with other parameters held fixed. In the parameter range studied, the concentrations in the reservoir are independent of time. Spatial variations of the chemical concentrations in the plane of the gel—that is, chemical patterns—are viewed with a video camera in reflected light in a band centred at 420 nm, where ferrocyanide absorbs strongly.